Synergistic humidity-responsive mechanical motion and proton conductivity in a cationic covalent organic framework

Gobinda Das, Dhanraj Shinde, Amrutha Melepurakkal, Manjusha Shelke, Bikash Garai, Philippe Bazin, Abdelhafid Ait Blal, Farah Benyettou, Thirumurugan Prakasam, Rasha Abdul Halim, et al.

Synergistic Humidity-Responsive Mechanical Motion and Proton Conductivity in a Cationic Covalent Organic Framework

Gobinda Das,[1,9] Dhanraj B Shinde,*[2] Amrutha Melepurakkal,[2,9] Manjusha V Shelke,[2] Bikash Garai,[1,3] Philippe Bazin,[4] Abdelhafid Aitblal,[4] Farah Benyettou,[1] Thirumurugan Prakasam,[1] Rasha Abdul Halim,[1] Fayrouz Abou Ibrahim, [1] Sudhir Kumar Sharma,[5] Sabu Varghese,[6] James Weston,[6] Ramesh Jagannathan,[5] Matthew Addicoat,[7] Felipe Gándara[8], Mark A. Olson,[10] Mohamad El-Roz,[4] Ali Trabolsi*[1,3]

[1] Chemistry Program, New York University Abu Dhabi (NYUAD), Saadiyat Island, United Arab Emirates

[2] Physical and Materials chemistry division, National Chemical laboratory, India, Pune-411008

[3] NYUAD Water Research Center, New York University Abu Dhabi (NYUAD), Saadiyat Island, United Arab Emirates

[4] Laboratoire Catalyse et Spectrochimie, CNRS, Ensicaen, Université de Caen, 6, Boulevard Maréchal Juin, 14050, Caen, France

[5] Engineering Division, New York University Abu Dhabi (NYUAD), United Arab Emirates

[6] CTP, New York University Abu Dhabi, 129188 Abu Dhabi, United Arab Emirates

[7] School of Science and Technology, Nottingham Trent University, Clifton Lane, NG11 8NS Nottingham, U.K.

[8] Instituto de Ciencia de Materiales de Madrid-CSIC, C. Sor Juana Inés de la Cruz 3, 28049 Madrid, Spain.

[9] Authors contributed equally.

[10] Department of Physical and Environmental Sciences, Texas A&M University Corpus Christi, 6300 Ocean Dr., Corpus Christi, TX 78412 USA.

*Correspondence: ali.trabolsi@nyu.edu, db.shinde@ncl.res.in

Lead contact: Gobinda Das

Bigger picture: Moisture as an energy source to trigger the mechanical motion of materials is an emerging research area of interest for the development of smart switches, artificial muscles and soft robots. Recently discovered periodic networks of covalent organic frameworks (COFs) provide a great platform to tune their structures with suitably responsive units and turn them into stimuli responsive. However, because of the overall hydrophobic character of conventional COFs, they lack the ability to engage in polar interactions, and limits the fabrication of moisture sensitive COF-based actuators. To overcome this challenge, we have developed a cationic, flexible COF film pre-functionalized with a water-sensitive guanidinium moiety. By exploiting the role of H-bonding in extended structure, we have successfully addressed two very important problems. Due to the H-bonding of the entrapped water molecules, our material enables a fast activation of mechanical motion that is faster that any previously reported porous framework materials. In addition to rapid activation, presence of H-bonded water molecules allows the creation of a highly efficient pathway for proton conduction within the framework. The designed

COF paves the way for innovative advances in the field of moisture-responsive conductive smart materials.

Summary: The design of flexible humidity responsive actuator-based materials capable of demonstrating substantial deformation and recovery within a short response time holds significant importance in the development of highly functional sensors and intelligent electronic systems. Despite the high demand for fast actuating materials, their fabrication process typically involves a complex and multistep approach under harsh conditions. Herein, we fabricated a self-standing cationic covalent organic framework (TG-DFP COF) film comprised of guanidinium and pyridine units via a simple one-step synthetic approach at room temperature. Due to the presence of H-bonding and ionic surface coverage throughout the COF network, this material facilitates the rapid adsorption and desorption of water vapor, leading to an ultrafast actuating response rate of less than one second. Apart from fast actuation, notably, under high humid conditions, the presence of trapped water molecules creates a significant number of H-bonding interactions within the COF network, resulting in an impressive proton conductivity of 2.8 mS cm^{-1}, which stands as one of the highest reported among cationic COFs. This study showcases a unique example of a 2D-ordered system that exhibits a synergistic combination of proton conductivity and shape-deforming capabilities with outstanding stability.

Introduction

Smart materials[1-4] capable of converting various external stimuli such as magnetic[5-7] or electric fields,[8-11] pH,[12-15] temperature,[16-19] solvent,[20-25] humidity,[26-31] and light[32-37] into mechanical deformation offer significant potential for making unprecedented advances in areas such as smart robots,[38] artificial muscles,[39-41] sensors,[42,43] and biomedical devices.[44] Among all existing external stimuli, humidity is an abundant, easily accessible, and renewable resource.[45] Since it is a purely natural, environmentally friendly stimulus, humidity-induced actuators are very interesting.[30,46-60] Humidity-induced actuators are used in a variety of potential applications, including thermal imaging,[61] sensing,[62] medical,[44] air control,[63] anti-counterfeiting,[64] and optical recording devices.[65] The development of fast-responding materials is critical to the development of actuators that can be used effectively in real-world applications.[66] The speed of actuation is a key parameter that greatly affects the overall performance and usability of such materials.[20,66,67] To date, most actuation materials have been limited to small organic molecules,[24,51,68] supramolecular gels,[39,62,66,69,70] metal-organic frameworks (MOFs),[71-74] and polymeric materials.[27,50,52,75] Despite their potential, it is worth noting that these materials exhibit poor mechanical properties under extreme conditions and suffer from slowed actuation speeds.[76] For

this reason, their practical applications in such systems are currently quite limited. Moreover, in polymeric systems, due to the lack of structural order, a complete understanding of the energy conversion process is never possible, as the interactions involved cannot be studied without a solid structural understanding.[77] To overcome the above difficulties, a stable actuating material with a defined chemical structure is required. Such properties can be achieved by crystalline materials such as metal/covalent organic frameworks (MOFs[72-74,76]/COFs[23,25,37]), whose ordered structural network can be used to understand and tune the energy conversion process, in addition to their application in various fields. In recent decades, moisture-responsive actuators in polymer,[31,60,62] liquid crystal,[27,64] and gel materials[51,56] have been well studied, but moisture-induced actuators in ordered networks such as MOFs[72-74] or COFs[28] are relatively rare. To date, only a hydrazide-based COF membrane decorated with polyethylene glycol (PEG) has been reported to exhibit moisture-induced triggering.[28] However, this material also exhibits a relatively low triggering rate and mechanical deformation compared to other existing polymeric actuators.[20,66,67] Moreover, the incorporation of PEG into the COF-42[78] backbone requires a time-consuming and complex multi-step synthesis process. Therefore, the development of an easy-to-process, moisture-responsive actuator with fast kinetics is of great interest. The key factor for the rapid activation of moisture-responsive actuators is the presence of suitable docking sites that facilitate the uptake and release of water. These docking sites provide an ideal environment for water molecules to interact with the material and enable rapid and reversible actuation in response to moisture changes. Compared to conventional COFs with neutral building blocks, ionic covalent organic frameworks (iCOFs)[79] with hydrophilic functional groups embedded in a layered network could promote strong interactions with water molecules to have a fast-responsive rate in response to a change in ambient humidity. In contrast to previous reports on humidity-controlled hybrid PEG -decorated COF actuators,[28] our goal in this study is to introduce a cationic guanidinium linker into the COF network. This enables rapid diffusion of water molecules within the frameworks due their hydrogen bonding with the guanidinium moiety. Based on this hypothesis, we have prepared a guanidinium-functionalized moisture-responsive free-standing cationic COF film (TG-DFP, Figure 1). This strategic modification improves the actuation performance at low humidity, and continuous self-movement was also achieved by placing the film on a wet filter paper.

In addition to the reversible, rapid activation in TG-DFP COF, the trapped water molecules inside the framework interestingly form a electrostatic interation with the cationic guanidinium moiety upon hydration. This interaction enables an inherent proton-conducting pathway that adds an

additional intriguing aspect to its functionality. To address the global energy crisis, proton-conducting materials have gained much attention due to their urgent need in proton exchange membrane fuel cells (PEMFCs) and other electronic devices.[80] To achieve high proton conductivity, researchers have usually adopted three main approaches to improve proton conductivity in ordered systems such as COFs[81,82] or MOFs[83]: 1) the use of a porous architecture to accommodate proton carriers such as inorganic acids (H_2SO_4 and H_3PO_4)[84]; 2) loading of the pore channel with neutral proton donors (e.g. imidazole,[85-88] ammonium cations,[89] etc.); and 3) modifying the pore walls of COFs[90]/MOFs[91] by functionalizing the ligands with proton-rich functional groups such as –COOH,[92] $–NH_2$,[93] and $–SO_3H$[94] to increase the acidity and hydrophilicity of the pore surface.

However, all these strategies encounter numerous synthetic challenges. Remarkably, the study of proton conductivity is rarely performed in nonporous systems,[95] and it is completely new in COFs.[96] Compared to other reported proton-conducting porous COFs[96] or MOFs,[97,98] our strategically designed ionic COF (TG-DFP) is very unique. Despite its nonporous nature, the free protons in the cationic guanidinium unit can easily migrate along the continuous hydrogen bonding pathway within the COF, resulting in a high proton conductivity under wet conditions of up to 2.08 mS cm^{-1}, which is higher than any reported cationic porous COFs[99,100] and comparable to the most proton-conducting neutral COFs reported so far under wet conditions.[100] The free-standing TG-DFP COF film was prepared by a one-pot imine condensation reaction between triamino guanidinium hydrochloride salt (TGH•Cl) and diformylpyridine (DFP) at room temperature. Our synthesis protocol does not require any additional synthesis effort compared to existing state-of-the-art actuator fabrication processes.[3,26-29,33] Due to the excellent water triggered actuation and high proton conductivity, the TG-DFP COF emerges as an utsanding framework model for investigating numerous innovative and functional applications.

Results and Discussion

Synthesis, characterization and Structural analysis

The guanidinium-functionalized TG-DFP COF film was prepared (Figure 1A) by the imine condensation reaction of pyridine-2,6-dicarbaldehyde (DFP) and triamino-guanidinium hydrochloride salt (TGH-Cl) in a mixture of ethanol and water (2:1, v/v) at room temperature. The formation of an imine bond in the TG-DFP COF film was confirmed by Fourier transform infrared (FT-IR) spectroscopy (Figure S1). The disappearance of the C=O stretching vibration at 1700 cm^{-1} of the DFP and the appearance of new C=N stretching vibrations at 1612

cm^{-1} confirmed the formation of imine bonds. ^{13}C cross-polarization magic angle spinning nuclear magnetic resonance spectroscopy (^{13}CPMAS NMR) in the solid-state spectrum (Figure S2) showed a resonance signal at 150 ppm, which further validated the formation of the C=N bond. Powder X-ray diffraction (PXRD) analysis of TG-DFP COF film was recorded to confirm the crystalline nature of the COF (Figure S3). We synthesized the material in powder form, the crystallinity is improved compared to the film form and the experimental PXRD pattern matched the simulated pattern (Figure S4a). Furthermore, we constructed several models based on honeycomb (**hcb**) layered structures, and optimized their geometry using universal force field energy minimization (Figure S3), finding good agreement for models within the monoclinic *Pm* space group (Figure 1B). The atomic positions of the structural models are now given in the revised SI. Accordingly, the position of the first peak in the experimental pattern is assigned to the (10–1), (100), and (001) Miller plane reflections, the position of the PXRD peaks and diffraction pattern are consistent with our previous reports on a TG-DFP-based gel or COF.[101,102] The position of the peak centered at $2\theta = 26.1°$ agrees well with the interlayer distance given by the (010) ad (020) planes for the eclipsed and staggered conformations, respectively. The broad feature observed in our TG-DFP COF network arises from the substantial charge repulsion between adjacent cationic sites, suggesting the absence of a specific stacking sequence. Similar observations have been reported for other guanidinium-based COFs in previous studies.[103] Furthermore, the structural order of the TG-DFP COF film was disrupted by the high degree of flexibility and non-planar structure of the guanidinium amine. Moreover, HRTEM analysis reveals well-defined lattice fringes, further confirming the periodic nature of the COF film. Unlike most reported COF-based films, the TG-DFP COF film is exceptionally transparent as it can be seen from Figure 2A. The morphology of the TG-DFP COF film was investigated by scanning electron microscopy (SEM, Figure 2B and S5), high-resolution transmission electron microscopy (HR-TEM, Figure 2C-E and S6), and atomic force microscopy (AFM, Figure 2F and S7).

The continuous and crack free nature of the smooth membrane surfaces is evident in the scanning electron microscopy (SEM) images (Figure 2B and S5 a). The cross-section images reveal that the thickness of the film is 2 ± 1 μm (Figure 2B). For microscopic analysis, the COF film was ultra-sonicated in ethanol for about 60 minutes. The resulting supernatant liquid was then drop-cast onto either a TEM grid (Cu) or an AFM silicon substrate. HR-TEM and AFM images showed that TG-DFP COF film has a laminated sheet-like morphology (Figures 2C–F, Figure S7). The ordered, oriented crystal lattice fringes (Figure 2E) of TG-DFP COF were confirmed by HR-TEM analysis at high magnification (Figure S4b). This was attributed to the

adjacent stacked 2D layer with a stacking distance of 0.38 nm (Figure S8); the stacking distance agrees well with the experimental wide-angle PXRD data. A final inspection of the AFM images (Figure 2f, Figure S7) revealed that the thickness of the obtained TG-DFP film is about 0.2 μm (as a film, Figure 2F), indicating that the COF network consists of multilayer stacked layers.

Mechanical behavior, humidity-induced mechanical actuation, and Mechanistic Investigation

To check the mechanical behavior of the TG-DFP COF film, a tensile stress-strain experiment was performed on the rectangular film using an MTI tensile stage (Figure 3A). The TG-DFP COF film is extremely durable and can be easily bent and folded (video S1) over several cycles without any mechanical stress (Figure 3B). The gage length was 25.4 mm, and the 5 N load cell was calibrated with loads from 10 to 90 g (0.098–0.883 N). The loading rate was 5 mm/minute. Stress was calculated through the cross-sectional area of the foil (10 mm and 3 mm by ruler, and 20 μm by cross-sectional SEM). The Young's modulus was calculated from the slope of the curve in the linear region and is in the range of 0.543 GPa to 1.27 GPa, which is comparable to other reported COF films.[28] In addition, we performed the water adsorption analysis of the COF film. The purpose of the water vapor adsorption capacity study was to evaluate the moisture-dependent behavior of the TG-DFP COF film. The water vapor adsorption behavior of the fully activated TG-DFP COF film exhibits type II isotherm, displaying considerable water sorption capacity at low and moderate relative humidity levels (%RH). This behavior is characteristic of hydrophilic materials, as shown Figure 3C. The TG-DFP COF achieves a maximum water uptake of 41.6 wt % at saturation. To evaluate the stability of the film under humid conditions, TG-DFP film was exposed to three consecutive cycles at equilibrium. The film showed high recyclability as observed by the almost identical water adsorption isotherms over three cycles (Figure S9). The water uptake capacity is comparable to the other porous COFs materials reported.[103,104]

To quantify the number of trapped water molecules and the thermal stability of the TG-DFP COF film (Figure S10), we performed thermo-gravimetry analysis (TGA). The TGA analysis shows that the COF network maintains thermal stability of up to 227 ºC. However, below 200 ºC, there is a significant weight loss (13 wt%, 17-140 ºC), which can be attributed to the presence of trapped water molecules within the framework. Through the TGA analysis and simulated structure, we have determined that the number of water molecules per unit cell is approximately 39.2.

The simulated structure clearly shows the remarkable flexibility of the TG-DFP COF structure (Figure S11a). Motivated by the flexibility or hydrophilicity (Figure 11b) of the framework and its sensitivity to water, we investigated the moisture-controlled actuation behavior (Figure 3d) of the TG-DFP COF film. The film is mechanically robust and flexible, allowing it to move and propagate rapidly in response to moisture. For mechanical actuation, the TG-DFP COF film (3 cm long, 2 μm thick) was positioned horizontally over a paper cup of warm water using tweezers (Figure 3D).

Upon approaching the top surface of the cup, the film curled up in response to the high humidity, bending significantly up to a bending angle of θ =175° (within 0.22 seconds) and then returning to its original shape once removed from the cup. The complete folding and unfolding process of the TG-DFP COF actuator occurred in only 0.69 seconds. The kinetics of the bending motion is measured by plotting the deflection angle of the film against time (Figure 3E). The rate of mechanical actuation is faster than any previously reported vapor- or moisture-induced COF, MOF, or cage-based actuator (supplemental information, Table S1). The process of curvature and recovery was repeated for multiple cycles (video S2). To verify the framework stability of the TG-DFP COF film, we performed PXRD (Figure S12) and ^{13}CPMAS NMR spectral analysis (Figure S13) on the COF film after it was exposed to wet conditions . The PXRD peak and ^{13}CPMAS NMR spectrum did not change under wet conditions, an indication of the extreme robustness of the COF film. In addition to reversible curvature and straightening of the COF film, the film also exhibits moisture-triggered motility that allows it to move from one location to another (Figure 3F, video S3). To test this self-mobility, we placed a squared film (size 2 cm × 2 cm) on a Whatman filter paper that was kept in a glass container filled with lukewarm water. In response to the moisture, the film spontaneously and continuously started moving. The locomotion of the film consisted of eight phases: (I) the film is initially flat, (II) it folds, (III) it takes a tubular shape, (IV) the film rolls up, (V) one side of the film becomes flat and the top side turns up, (VI) then the film rolls up again, (VII) then the film tilts, and finally (VIII) the film rolls with the top side down. Figure 3F shows a schematic representation of a complete cycle. In addition, the actuating behavior of the TG-DFP COF film was tested in other polar and nonpolar solvents (ethanol, DCM, acetone, THF, and hexane). The film showed no mechanical response in these solvents (video S4-S6), which confirms that the bending behavior is very selective for water moisture. The mechanical bending or rolling of the COF film in response to humidity is driven by the absorption and desorption of water molecules on the film's surface. The mechanism responsible for humidity responsiveness primarily involves a variety of non-covalent interactions

between the material and water molecules, including hydrogen bonding, electrostatic interactions, and ion-dipole interactions. To confirm our hypothesis, first we conducted dynamic vapor sorption (DVS) experiments at ambient temperature, ranging from 0% to 100% relative humidity (RH), using dry nitrogen as the carrier gas. The results, illustrated in Figure 3C and Figure S8, demonstrate that the TG-COF film exhibited a robust humidity response with excellent cyclic stability. The uneven absorption of water by the COF-film triggers asymmetric swelling, leading to the deformation. When the film is on a moist substrate, the expansion of the surface of the film facing the substrate caused by water adsorption exceeds that of the upper surface causing the film to curl up. This bending of the TG-DFP film in response to moisture is illustrated by a simple experiment shown in Figure. S14. When a piece of the rectangular film is placed on a bare human palm, it absorbs the moisture from perspiration, causing it to curl and develop noticeable curvature. The film quickly returns to its original flat shape when placed on the dry surface of a palm covered with a rubber glove. Moreover, Ion-dipole interactions between water and the halide counterions reduces the ion's ability to neutralize the charge of the organic cation. It is therefore very possible that adsorbed water also increases the cationic charge on the side of the film where the water adsorbs. The coulombic repulsion on that side should cause the material curl and flip in the opposite direction, as the units try to increase the distance between them. This effect would also explain the structural changes observed by FTIR.

To understand the mechanism of actuation, we performed additional experiments by coupling thermogravimetry with FTIR analysis (Figure 4, Figure S15-16).[105,106] This allows simultaneous observation of the evolution of the sample mass (Δm resolution=1μg; Figure 4A) and its IR spectra (Figure 4B) under different conditions. Thus, important and quantitative information about the adsorption mechanism, the structural change, the extinction coefficient of the corresponding bands, and the adsorption enthalpy (Figure 5) can be obtained. Figure 4A shows the mass gain of the films and the evolution of their FTIR spectra after 6 wet (RH = 4%) and dry cycles at 25°C. The results show a high reversibility during the six cycles. The IR analysis also shows a reversible shift of some characteristic vibrational bands (1700 cm^{-1}-800 cm^{-1}) of the TG-DFP structure (Figures 4 B, C, and Figure S14) with water adsorption and desorption (band 3378 cm^{-1}). However, the original spectra (Figure S15 in SI) show that some bands of the structure are not affected by the water adsorption, such as the band at 1707 cm^{-1} assigned to the carbonyl vibration of the terminal DFP group of the structure. It is noteworthy that the band associated with C=O vibration (approximately 1707 cm^{-1}) is still present in the IR spectra of the COFs, although its intensity is negligible compared to that of DFP (Figure S1). This could be

ascribed to the terminal aldehyde groups situated at the edges of the COFs. In the ^{13}C CP/MAS spectrum of the TG-DFP COF film (Figure S2), the presence of the C=O group could not be detected. A similar observation has been reported in other COFs as well.[107] It should be noted that 50% of the amount of water can be reversibly adsorbed or desorbed at 25°C and RH = 4% with respect to the activated sample at 100°C, showing that the samples can respond to water moisture without having to be thermally activated first.

FTIR experiments clarified how the structure was modified during the process by observing a shift of the structural bands after water adsorption: The shift of the main characteristic vibrational bands of the TG-DFP film may be mainly due to two possible water effects: a direct effect due to hydrogen bonding between the adsorbed water molecules and the corresponding functional groups of the film (e.g., the bands affected by the presence of water in Figure 4B could be assigned as follows: 3389 cm^{-1} (v(OH)), 2530 cm^{-1} (v(NH)), 1286 cm^{-1} and 1327 cm^{-1} (aromatic C-N stretching vibration), 804 cm^{-1} and 821 cm^{-1} (v(CH)).[108,109] Indirect effects of hydrogen bonding can lead to changes in bond length, bond angle, and electron distribution of bonded atoms within a molecule. These changes, in turn, affect the vibrational frequencies of neighboring functional groups, indicating changes in the molecular structure of the material. Hydrogen bonding can have a significant impact on the overall properties and behavior of a material due to these structural changes. To better distinguish between these two phenomena, we performed a two-dimensional correlation FTIR spectroscopy experiment [110] using D_2O and H_2O (Figure S17), respectively, with similar RH values. This correlation allows us to distinguish the bands shifted due to water adsorption by hydrogen bonds (shift to the lower wavenumbers in D_2O) from those due to changes in molecular structure (bands crossing the diagonal as no change is observed between the two experiments). The results (Figure 4D-F) show that the position of the bands around 1430 cm^{-1}, 1300 cm^{-1}, and 930 cm^{-1} does not change between D_2O and H_2O, unlike the other bands. These bands are likely to be associated with the (CH) and (C-N-C) bands of the aromatic moiety of the TG-DFP COF structure.[105] Thus, the shift observed in these bands has nothing to do with hydrogen bonding but more likely with the change in molecular structure when the film is exposed to moisture. Moreover, the shift in certain structural bands serves as direct evidence that water adsorption promotes microscopic modifications, which manifest as a macroscopic mechanical response in the materials. This phenomenon highlights the significance of the interaction between water and COFs as the primary driving force. The stress-strain behavior following exposure to water typically emerges from intricate electrostatic interactions and hydrogen bonding between the material and water molecules.

Finally, we measured the bending curvature of the film under different relative humidities (Figure S18). Finally, we measured the bending curvature of the film at different relative humidities (Figure S18). Under ambient conditions (RH = 51%), the TG-DFP COF film is flat, and this state (curvature 0) is defined as the reference point. With an increase in RH from 51% to 95%, the curvature gradually increases and reaches a maximum of 0.144 mm^{-1} at 95% RH. All experimental evidence clearly indicates that the actuation mechanism involves the formation of a thin hydrated surface layer that causes the entire film bend when exposed to the humidity gradient. In order to obtain thermodynamic information about the adsorption of water in TG-DFP, three isotherms were performed at different temperatures: 20, 50, and 70 °C. All measurements and simulations are shown in Figure 5. The optical isotherms (area of the OH band at 3380 cm^{-1}versus H_2O pressure) are shown in Figure 5A. The isotherms were modeled at the various temperatures using the least squares method (Figure 5C). Each modeled isotherm is the combination of two curves. The first is proportional to the curve with respect to the band height of 1286 cm^{-1} (an identical proportional factor was used for the three temperatures), as shown in Figure 5B. The second curve is characterized by a classical Langmuir model. For high pressures, the interaction is weaker. Using a method described in the literature, it is possible to determine the thermodynamic values (ΔH) of H_2O adsorption considering a combination of the Van't Hoff and Langmuir equations for the three temperatures. Thus, we determined an enthalpy of 43–44 kJ mol^{-1} for the weak interaction, which corresponds to the standard liquefaction enthalpy of water. The determination of the heat of adsorption of water at low pressure (relatively strong adsorption) is not possible because we have two simultaneous phenomena: the heat of adsorption of water and the heat relative to the structural evolution of the material. The evolution of the amount of adsorbed water (area of the OH band at 3380 cm^{-1}) during the cycles of H_2O (5 mbar/1 h) and H_2O (0 mbar/2 h) in Ar (20 cm^3 min^{-1}) at 20 °C (Figure 5 D) shows a fluctuation between 150 and 270 (unit of area). This range of variation is symbolized by the arrows in Figures 5c and 5d, and is clearly attributed to the variation of the weakly adsorbed water at 5 mbar and 20 °C. Therefore, the strong interaction between water and the "NH" sites remains irreversibly adsorbed under ambient conditions.

To understand the humidity-dependent actuation mechanism of 2D-COFs at the molecular level, PXRD is an extremely valuable technique, the use for which is extensively documented in the literature. PXRD analysis (Figure S19) clearly shows that the intensity of the characteristic diffraction peak at 5.8° decreases and the π-π stacking peak becomes broader, while the d-spacing value shifts to higher 2θ values. This observation clearly confirms that the formation of

a water network within the framework results in an in-plane shrinkage of the film. Under humid conditions, the reduced layer spacing implies a weakening of the initial intermolecular hydrogen bonds between the COF layers, inducing the bending of the film. A similar observation has also been noted for previously reported humidity responsive COFs.[28]

Proton Conductivity of the TG-DFP COF film

The remarkable mechanical strength, ionicity, and presence of infinite H-bonding within the COF network motivated us to investigate the proton conductivity of the TG-DFP COF film. When it comes to proton conductivity, most COFs in powder form face the problem of being very fragile during pellet production.[111] The application of high pressure in this process can lead to structural weaknesses that can result in poor performance under fuel cell operating conditions. Interestingly, the TG-DFP COF film we developed with superior flexibility and a large charged backbone showed higher water uptake at room temperature, resulting in the formation of interconnected ion-water channels, which are highly beneficial for proton conductivity. Accordingly, the proton conductivity study shows that the TG-DFP COF film has a conductivity of 0.372 mS cm^{-1} at 20% RH (Figure 6A). At a fixed temperature, the conductivity value increases dramatically with increasing humidity, reaching a conductivity of 2.8 mS cm^{-1} (Figure 6B) at a high humidity of 99% RH, which is the highest of all proton-conducting cationic COFs[99,100] and comparable to other neutral COFs[84,94,112] (supplemental information Table S2) reported to date. The impact of relative humidity on conductivity can be elucidated as follows: an increase in relative humidity results in a greater presence of water molecules participating in conduction. This, in turn, facilitates the development of dense hydrogen bonding networks, establishing an effective pathway for proton hopping and subsequently increasing the proton conductivity. The high conductivity under humid conditions clearly indicates that proton conductivity is a surface-confined, water-assisted process.[113] To understand the proton transport mechanism and activation energy, the proton conductivity of the TG-DFP COF film was also measured at different temperatures from 20–100 °C (Figure 6C, Figure S20). The conductivity value of the TG-DFP COF film was found to be 0.915 mS cm^{-1} at 20 °C, and increased to 2.08 mS cm^{-1} at 100 °C. The activation energy determined from the temperature-dependent conductivity profiles is 4.4 kJ mol^{-1} (Figure S21), and the low activation energy of the TG-DFP COF film is lower than 10 kJ mol^{-1}, indicating that the proton transfer within the COF network obeys the Grotthuss mechanism[114] and confirms presence of trapped water molecules could be useful for the proton transfer (Figure 6D). There is indeed the possibility of hydrogen bonding with the guanidinium core within the framework. However, our simulated structure with water

molecules (Figure S22) clearly confirms that the water molecules form a hydration sphere around the chloride ions, which are mainly located near the guanidinium units by ionic interaction. The proton-conducting mechanistic pathway via anion-water hydrogen bonding is well documented in another cationic system as reported by the Mukhopadhyay group in their work on ionic Box.[113] To see the effect of other counter anions, we attempted to synthesize a TG-DFP COF film with the PF6 anion by anion exchange. Unfortunately, due to the larger size of the counter anion, we were unable to obtain a stable COF film. The resulting film was somewhat brittle in nature (Figure S23) and unsuitable for conductivity studies. In addition, the PXRD pattern of the broken TG-DFP-COF film appeared completely amorphous.

Thickness dependent Proton Conductivity and Fuel cell applications of the TG-DFP COF film

To understand how film thickness affects both mechanical actuation and proton conductivity, we fabricated TG-DFP COF films with different thicknesses. The thickness of the TG-DFP COF film we prepared ranged from 2 - 50 μm, as confirmed by the cross-sectional analysis of the SEM images (Figure 7 A-E). Remarkably, we observed a notable correlation between the film thickness and the bending curvature and proton conductivity. In particular, thinner films exhibited larger bending curvatures (Figure 7F). Furthermore, the thicker films exhibited slower moisture diffusion within the COF network, resulting in a reduction in bending curvature. The thickness of a proton conducting film plays a crucial role in determining its performance under the actual operating conditions of fuel cell. Since the TG-DFP COF exhibits high proton conductivity under humid conditions, we conducted electrochemical impedance spectroscopy (EIS) on all films under high humidity (RH = 98%). The EIS analysis shows that the proton conductivity decreases from 2.8 mS^{-1} to 0.68 mS^{-1} as the film thickness increases (Figure 7G-H). This is due to the fact that the continuity of ionic channels decreases with increasing film thickness, which leads to disruption in the mean free path for proton diffusion.[82]

To evaluate the potential application of the TG-DFP COF film, we conducted a study utilizing microbial fuel cells (MFCs).[115] MFCs are devices that can generate energy through microbial activity. Typically, MFCs consist of an anode and a cathode chamber separated by a membrane. The anode chamber contains a carbon felt anode on which an E-coli biofilm formation occurs, which is submerged in a culture medium. The cathode chamber contains a carbon felt electrode and is filled with ferricyanide ($Fe(CN)_6$) catholyte. These chambers are separated by a proton-conducting membrane. Before the measurement, the solution from anodic side is purged with nitrogen gas for 30 min to remove the dissolved oxygen and anodic chamber is tightly sealed to

maintain the anaerobic condition while performing MFC experiment. Both MFC experiments are performed at ~25 °C. In our investigation, we compared a commercially available membrane with the TG-DFP COF film. The first experiment utilized the two Nafion 212 membrane (Figure 7I), while the second employed a modified sandwich model (Nafion 212/TG-DFP COF/Nafion 212) (Figure 7J). We measured the power and current density using linear sweep voltammetry (LSV) ranging from open circuit voltage (OCV) to 0 V at a scan rate of 1 mV s^{-1}. The results showed that the experiment with two Nafion 212 had a power density of about 47 mW m^{-2}, with a maximum OCV of 430 mV. The experiments with the sandwich model showed a power density of 85 mW m^{-2} and an OCV of about 600 mV. These results indicate that the sandwich model incorporating the TG-DFP COF film membrane has a higher OCV and power density compared to Nafion membranes due to the comparable conductivity, thick biofilm formation on anode electrode and minimal crossover of ionic species. To see the effect of other counter anions, we attempted to synthesize a TG-DFP COF film with the PF6 anion by anion exchange. Unfortunately, due to the larger size of the counter anion, we were unable to obtain a stable COF film. The resulting film was somewhat brittle in nature (Figure S23) and unsuitable for conductivity studies. In addition, the PXRD pattern of the broken TG-DFP-COF film appeared completely amorphous.

Conclusions

In summary, we have succeeded in developing a moisture-driven cationic COF actuator, TG-DFP, with high proton conductivity, mechanical capabilities, and driving power. Unlike other reported COFs, we fabricated our COF actuator at room temperature without the need for costly or complicated polymeric additives. Our strategically designed actuator exhibits rapid deformation (175°/0.2 s), with fast actuation kinetics than any previously reported ordered COFs, MOFs, or cages. The presence of entrapped water molecules and a significant number of H-bonds within the COF network plays a crucial role in its mechanical motion and intrinsic proton conductivity, allowing it to reach up to 2.8 mS cm^{-1} under 99% humidity RH. It is clear that the incorporation of ionic guanidinium units, which function as water-sensitive units in the COF network, can be an excellent approach for the development of conductive moisture-responsive materials, thus advancing the development of advanced smart materials.

EXPERIMENTAL PROCEDURES

Resource availability

Lead contact

Further information and requests for resources should be directed to and will be fulfilled by the lead contact, Ali Trabolsi (ali.trabolsi@nyu.edu)."

Materials availability

All materials generated in this study are available from the lead contact without restriction.

Data and code availability

This study did not generate any datasets.

Synthesis, Characterization, and proton conductivity experiments

The full experimental details; NMR, and operando IR data; X-ray crystallographic structure determination; Water adsorption analysis and TGA data; and theoretical calculation results can be found in the supplemental information.

SUPPLEMENTAL INFORMATION

Supplementary information, comprising materials and analytical methods, material synthesis and structural details.

ACKNOWLEDGMENTS

This work was supported by New York University Abu Dhabi and the NYUAD Water Research Center, funded by Tamkeen under the NYUAD Research Institute Award (project CG007). We thank NYUAD for their generous support for the research program. DBS and MVS acknowledges the support from DBT Ramalingaswami research grant project GAP332626 and Australian Alumni grant scheme project GAP335726. The research work was carried out by using the Core Technology Platform resources at NYUAD. M.A. acknowledges support from EPSRC, EP/S015868/1, and HPC resources on Thomas viathe Materials Chemistry Consortium, EP/P020194. M. El-Roz acknowledge the Normandy Region and the European union for the financial support (project SuntoChem).

AUTHOR CONTRIBUTIONS

G.D. and A.T. conceptualized and designed the experiments, while G.D. and T.P. synthesized the initial materials. G.D. conducted the COF synthesis, with structural characterizations performed by G.D. and T.P. Proton conductivity and fuel cell experiments were conducted by D.B.S, M.V.S, and A.M., while M.A. and F.G. undertook the computational investigation. Operando FT-IR studies were conducted by F.B., A.A., and M.E.R., with AFM studies of the COFs performed by S.K.S. and R.J. HRTEM analysis was carried out by F.B., and solid-state NMR experiments and data analysis were conducted by S.V. Mechanical actuation studies were performed by B.G., and water adsorption measurements were conducted by R.G.A. M.A.O. contributed to manuscript preparation and provided valuable input. G.D., F.A.I., A.T., and M.A.O. were responsible for manuscript writing, with all authors contributing to manuscript review and commentary.

DECLARATION OF INTERESTS

The authors declare no competing financial interest.

References:

1. Hu, L., Wan, Y., Zhang, Q., and Serpe, M.J. (2020). Harnessing the Power of Stimuli-Responsive Polymers for Actuation. Adv. Funct. Mater. *30*, 1903471.
2. Hauck, M., Saure, L.M., Zeller-Plumhoff, B., Kaps, S., Hammel, J., Mohr, C., Rieck, L., Nia, A.S., Feng, X., Pugno, N.M., et al. Overcoming Water Diffusion Limitations in

Hydrogels via Microtubular Graphene Networks for Soft Actuators. Adv. Mater. *n/a*, 2302816.
3. Nguyen, V.H., Tabassian, R., Oh, S., Nam, S., Mahato, M., Thangasamy, P., Rajabi-Abhari, A., Hwang, W.-J., Taseer, A.K., and Oh, I.-K. (2020). Stimuli-Responsive MXene-Based Actuators. Adv. Funct. Mater. *30*, 1909504.
4. Apsite, I., Salehi, S., and Ionov, L. (2022). Materials for Smart Soft Actuator Systems. Chem. Rev. *122*, 1349-1415.
5. Yang, Z., and Zhang, L. (2020). Magnetic Actuation Systems for Miniature Robots: A Review. Adv. Intell. Syst. *2*, 2000082.
6. Fuhrer, R., Athanassiou, E.K., Luechinger, N.A., and Stark, W.J. (2009). Crosslinking Metal Nanoparticles into the Polymer Backbone of Hydrogels Enables Preparation of Soft, Magnetic Field-Driven Actuators with Muscle-Like Flexibility. Small *5*, 383-388.
7. Xiong, Z., Zheng, C., Jin, F., Wei, R., Zhao, Y., Gao, X., Xia, Y., Dong, X., Zheng, M., and Duan, X. (2018). Magnetic-field-driven ultra-small 3D hydrogel microstructures: Preparation of gel photoresist and two-photon polymerization microfabrication. Sens. Actuators B: Chem.
8. Xu, C., Faul, C.F.J., Taghavi, M., and Rossiter, J. (2023). Electric Field-Driven Dielectrophoretic Elastomer Actuators. Adv. Funct. Mater. *33*, 2208943.
9. Xiao, Y.-Y., Jiang, Z.-C., Hou, J.-B., Chen, X.-S., and Zhao, Y. (2022). Electrically driven liquid crystal network actuators. Soft Matter *18*, 4850-4867.
10. Ahn, J., Gu, J., Choi, J., Han, C., Jeong, Y., Park, J., Cho, S., Oh, Y.S., Jeong, J.-H., Amjadi, M., and Park, I. (2022). A Review of Recent Advances in Electrically Driven Polymer-Based Flexible Actuators: Smart Materials, Structures, and Their Applications. Adv Mater Technol *7*, 2200041.
11. Xu, S., Chen, Y., Hyun, N.-s.P., Becker, K.P., and Wood, R.J. (2021). A dynamic electrically driven soft valve for control of soft hydraulic actuators. Proc. Nat. Acad. Sci. *118*, e2103198118.
12. Ma, C., Lu, W., Yang, X., He, J., Le, X., Wang, L., Zhang, J., Serpe, M.J., Huang, Y., and Chen, T. (2018). Bioinspired Anisotropic Hydrogel Actuators with On–Off Switchable and Color-Tunable Fluorescence Behaviors. Adv. Funct. Mater. *28*, 1704568.
13. Houben, S.J.A., Lugger, S.J.D., van Raak, R.J.H., and Schenning, A.P.H.J. (2022). A pH-Responsive Liquid Crystal Hydrogel Actuator with Calcium-Induced Reprogrammable Shape Fixing. ACS Appl. Polym.Mater. *4*, 1298-1304.
14. Wu, B.-Y., Le, X.-X., Jian, Y.-K., Lu, W., Yang, Z.-Y., Zheng, Z.-K., Théato, P., Zhang, J.-W., Zhang, A., and Chen, T. (2019). pH and Thermo Dual-Responsive Fluorescent Hydrogel Actuator. Macromol. Rapid Commun. *40*, 1800648.
15. Zarzar, L.D., Kim, P., and Aizenberg, J. (2011). Bio-inspired Design of Submerged Hydrogel-Actuated Polymer Microstructures Operating in Response to pH. Adv. Mater. *23*, 1442-1446.
16. Liu, H., Jia, X., Liu, R., Chen, K., Wang, Z., Lyu, T., Cui, X., Zhao, Y., and Tian, Y. (2022). Multifunctional gradient hydrogel with ultrafast thermo-responsive actuation and ultrahigh conductivity. J. Mater. Chem. A *10*, 21874-21883.
17. Kang, D.J., An, S., Yarin, A.L., and Anand, S. (2019). Programmable soft robotics based on nano-textured thermo-responsive actuators. Nanoscale *11*, 2065-2070.
18. Belmonte, A., Ussembayev, Y.Y., Bus, T., Nys, I., Neyts, K., and Schenning, A.P.H.J. (2020). Dual Light and Temperature Responsive Micrometer-Sized Structural Color Actuators. Small *16*, 1905219.
19. Jiang, S., Liu, F., Lerch, A., Ionov, L., and Agarwal, S. (2015). Unusual and Superfast Temperature-Triggered Actuators. Adv. Mater. *27*, 4865-4870.

20. Zhao, Q., Dunlop, J.W.C., Qiu, X., Huang, F., Zhang, Z., Heyda, J., Dzubiella, J., Antonietti, M., and Yuan, J. (2014). An instant multi-responsive porous polymer actuator driven by solvent molecule sorption. Nat. Commun. *5*, 4293.
21. Sun, Q., Ayela, C., and Thuau, D. (2023). Solvent-Driven Biomimetic Soft Sensors and Actuators. Adv. Mater. Interfaces *10*, 2201349.
22. Lin, E., Wang, Z., Zhao, X., Liu, Z., Yan, D., Jin, F., Chen, Y., Cheng, P., and Zhang, Z. (2022). A class of rigid–flexible coupling crystalline crosslinked polymers as vapomechanical actuators. Angew. Chem. *134*, e202117390.
23. Wang, Z., Yu, Q., Huang, Y., An, H., Zhao, Y., Feng, Y., Li, X., Shi, X., Liang, J., and Pan, F. (2019). PolyCOFs: a new class of freestanding responsive covalent organic framework membranes with high mechanical performance. ACS Cent. Sci. *5*, 1352-1359.
24. Alimi, L.O., Fang, F., Moosa, B., Ding, Y., and Khashab, N.M. (2022). Vapor-Triggered Mechanical Actuation in Polymer Composite Films Based on Crystalline Organic Cages. Angew. Chem.Int. Ed. *61*, e202212596.
25. Liu, X., Li, J., Gui, B., Lin, G., Fu, Q., Yin, S., Liu, X., Sun, J., and Wang, C. (2021). A Crystalline Three-Dimensional Covalent Organic Framework with Flexible Building Blocks. J. Am. Chem. Soc. *143*, 2123-2129.
26. Wang, J., Ma, H., Liu, Y., Xie, Z., and Fan, Z. (2021). MXene-Based Humidity-Responsive Actuators: Preparation and Properties. ChemPlusChem *86*, 406-417.
27. de Haan, L.T., Verjans, J.M.N., Broer, D.J., Bastiaansen, C.W.M., and Schenning, A.P.H.J. (2014). Humidity-Responsive Liquid Crystalline Polymer Actuators with an Asymmetry in the Molecular Trigger That Bend, Fold, and Curl. J. Am. Chem. Soc. *136*, 10585-10588.
28. Mao, T., Liu, Z., Guo, X., Wang, Z., Liu, J., Wang, T., Geng, S., Chen, Y., Cheng, P., and Zhang, Z. (2023). Engineering Covalent Organic Frameworks with Polyethylene Glycol as Self-Sustained Humidity-Responsive Actuators. Ange. Chem. *135*, e202216318.
29. Ge, Y., Wang, H., Xue, J., Jiang, J., Liu, Z., Liu, Z., Li, G., and Zhao, Y. (2021). Programmable Humidity-Responsive Actuation of Polymer Films Enabled by Combining Shape Memory Property and Surface-Tunable Hygroscopicity. ACS Appl. Mater. Interfaces *13*, 38773-38782.
30. Li, B., Duan, X., Cheng, D., Chen, X., Gao, Z., Ren, W., Shao, K.-Z., and Zang, H.-Y. (2023). Controllable Transition Metal-Directed Assembly of [Mo2O2S2]2+ Building Blocks into Smart Molecular Humidity-Responsive Actuators. J. Am. Chem. Soc. *145*, 2243-2251.
31. Arazoe, H., Miyajima, D., Akaike, K., Araoka, F., Sato, E., Hikima, T., Kawamoto, M., and Aida, T. (2016). An autonomous actuator driven by fluctuations in ambient humidity. Nat. Mater. *15*, 1084-1089.
32. Li, L., Scheiger, J.M., and Levkin, P.A. (2019). Design and Applications of Photoresponsive Hydrogels. Adv. Mater. *31*, 1807333.
33. Stoychev, G., Kirillova, A., and Ionov, L. (2019). Light-Responsive Shape-Changing Polymers. Adv. Opt. Mater. *7*, 1900067.
34. Gelebart, A.H., Mulder, D.J., Vantomme, G., Schenning, A.P., and Broer, D.J. (2017). A rewritable, reprogrammable, dual light-responsive polymer actuator. Angew. Chem. *129*, 13621-13624.
35. Verpaalen, R.C.P., Pilz da Cunha, M., Engels, T.A.P., Debije, M.G., and Schenning, A.P.H.J. (2020). Liquid Crystal Networks on Thermoplastics: Reprogrammable Photo-Responsive Actuators. Angew. Chem. Int. Ed. *59*, 4532-4536.

36. Jiang, Z., Tan, M.L., Taheri, M., Yan, Q., Tsuzuki, T., Gardiner, M.G., Diggle, B., and Connal, L.A. (2020). Strong, self-healable, and recyclable visible-light-responsive hydrogel actuators. Angew. Chem. *132*, 7115-7122.
37. Guo, X., Mao, T., Wang, Z., Cheng, P., Chen, Y., Ma, S., and Zhang, Z. (2020). Fabrication of Photoresponsive Crystalline Artificial Muscles Based on PEGylated Covalent Organic Framework Membranes. ACS Cent. Sci. *6*, 787-794.
38. Hines, L., Petersen, K., Lum, G.Z., and Sitti, M. (2017). Soft Actuators for Small-Scale Robotics. Adv. Mater. *29*, 1603483.
39. Greene, A.F., Danielson, M.K., Delawder, A.O., Liles, K.P., Li, X., Natraj, A., Wellen, A., and Barnes, J.C. (2017). Redox-Responsive Artificial Molecular Muscles: Reversible Radical-Based Self-Assembly for Actuating Hydrogels. Chem. Mater. *29*, 9498-9508.
40. Mirvakili, S.M., and Hunter, I.W. (2018). Artificial Muscles: Mechanisms, Applications, and Challenges. Adv. Mater. *30*, 1704407.
41. Iwaso, K., Takashima, Y., and Harada, A. (2016). Fast response dry-type artificial molecular muscles with [c2] daisy chains. Nat. chem. *8*, 625-632.
42. Chen, L., Weng, M., Zhou, P., Huang, F., Liu, C., Fan, S., and Zhang, W. (2019). Graphene-Based Actuator with Integrated-Sensing Function. Adv. Funct. Mater. *29*, 1806057.
43. Yeo, J.C., Yap, H.K., Xi, W., Wang, Z., Yeow, C.-H., and Lim, C.T. (2016). Flexible and Stretchable Strain Sensing Actuator for Wearable Soft Robotic Applications. Adv. Mater. Technol *1*, 1600018.
44. Zhang, Z., Wang, Y., Wang, Q., and Shang, L. (2022). Smart Film Actuators for Biomedical Applications. Small *18*, 2105116.
45. Pu, W., Wei, F., Yao, L., and Xie, S. (2022). A review of humidity-driven actuator: toward high response speed and practical applications. J. Mater. Sci. *57*, 12202-12235.
46. Wang, W., Wang, S., Xiang, C., Liu, S., Li, M., and Wang, D. (2021). Graphene Oxide/Nanofiber-Based Actuation Films with Moisture and Photothermal Stimulation Response for Remote Intelligent Control Applications. ACS Appl. Mater. Interfaces *13*, 48179-48188.
47. Carter, N.A., and Grove, T.Z. (2018). Protein Self-Assemblies That Can Generate, Hold, and Discharge Electric Potential in Response to Changes in Relative Humidity. J. Am. Chem.Society *140*, 7144-7151.
48. He, Y., Kong, K., Guo, Z., Fang, W., Ma, Z., Pan, H., Tang, R., and Liu, Z. (2021). A highly sensitive, reversible, and bidirectional humidity actuator by calcium carbonate ionic oligomers incorporated poly (vinylidene fluoride). Adv. Funct. Mater. *31*, 2101291.
49. Yue, X., Dong, C., Wang, Y., Cui, Z., Ren, Z., and Guan, Z.-H. (2023). Three birds with one stone: Design and synthesis of polyurethane actuator for executing heat, light and humidity triggered deformation. Chem. Eng. J. *457*, 141290.
50. Druvari, D., Kyriakopoulou, F., Lainioti, G.C., Vlamis-Gardikas, A., and Kallitsis, J.K. (2023). Humidity-Responsive Antimicrobial Membranes Based on Cross-Linked Copolymers Functionalized with Ionic Liquid Moieties. ACS Appl. Mater. Interfaces *15*, 11193-11207.
51. Lan, R., Gao, Y., Shen, C., Huang, R., Bao, J., Zhang, Z., Wang, Q., Zhang, L., and Yang, H. (2021). Humidity-Responsive Liquid Crystalline Network Actuator Showing Synergistic Fluorescence Color Change Enabled by Aggregation Induced Emission Luminogen. Adv. Funct. Mater. *31*, 2010578.
52. Liu, Y., Xu, B., Sun, S., Wei, J., Wu, L., and Yu, Y. (2017). Humidity- and Photo-Induced Mechanical Actuation of Cross-Linked Liquid Crystal Polymers. Adv. Mater. *29*, 1604792.

53. Zhang, L., Zhang, Y., Li, F., Yan, S., Wang, Z., Fan, L., Zhang, G., and Li, H. (2019). Water-Evaporation-Powered Fast Actuators with Multimodal Motion Based on Robust Nacre-Mimetic Composite Film. ACS Appl. Mater. Interfaces *11*, 12890-12897.
54. Gao, X., Zhang, L., Wang, S., Yang, T., and Li, H. (2021). Soft Untethered Robots and Grippers Based on Humidity-Gated Magnetic-Responsive Film Actuators. ACS Appl. Polym. Mater. *3*, 4726-4734. 10.1021/acsapm.1c00978.
55. Héraly, F., Zhang, M., Åhl, A., Cao, W., Bergström, L., and Yuan, J. (2022). Nanodancing with Moisture: Humidity-Sensitive Bilayer Actuator Derived from Cellulose Nanofibrils and Reduced Graphene Oxide. Adv. Intel. Syst. *4*, 2100084.
56. Lv, C., Xia, H., Shi, Q., Wang, G., Wang, Y.-S., Chen, Q.-D., Zhang, Y.-L., Liu, L.-Q., and Sun, H.-B. (2017). Sensitively Humidity-Driven Actuator Based on Photopolymerizable PEG-DA Films. Adv. Mater. Interfaces *4*, 1601002.
57. Troyano, J., Carné-Sánchez, A., Pérez-Carvajal, J., León-Reina, L., Imaz, I., Cabeza, A., and Maspoch, D. (2018). A Self-Folding Polymer Film Based on Swelling Metal–Organic Frameworks. Angew. Chem. Int. Ed. *57*, 15420-15424.
58. Yang, L., Cui, J., Zhang, L., Xu, X., Chen, X., and Sun, D. (2021). A Moisture-Driven Actuator Based on Polydopamine-Modified MXene/Bacterial Cellulose Nanofiber Composite Film. Adv. Funct. Mater. *31*, 2101378.
59. Wang, J., Liu, Y., Cheng, Z., Xie, Z., Yin, L., Wang, W., Song, Y., Zhang, H., Wang, Y., and Fan, Z. (2020). Highly Conductive MXene Film Actuator Based on Moisture Gradients. Angew. Chem. Int. Ed. *59*, 14029-14033.
60. Zhao, Z., Hwang, Y., Yang, Y., Fan, T., Song, J., Suresh, S., and Cho, N.-J. (2020). Actuation and locomotion driven by moisture in paper made with natural pollen. Proc. Nat. Acad. Sci. *117*, 8711-8718. doi:10.1073/pnas.1922560117.
61. Xiang, C., Wang, W., Liu, S., Huang, Y., Li, M., and Wang, D. (2023). Humidity-stimulated film actuator with dual-responsive of bending deformation and discoloration. Sens. Actuators B: Chem. *380*, 133344.
62. Verpaalen, R.C.P., Souren, A.E.J., Debije, M.G., Engels, T.A.P., Bastiaansen, C.W.M., and Schenning, A.P.H.J. (2020). Unravelling humidity-gated, temperature responsive bilayer actuators. Soft Matter *16*, 2753-2759. 10.1039/D0SM00030B.
63. Bernat, J., and Kolota, J. (2018). Adaptive observer-based control for an IPMC actuator under varying humidity conditions. Smart Mater. Struct. *27*, 055004.
64. Lan, R., Shen, W., Yao, W., Chen, J., Chen, X., and Yang, H. (2023). Bioinspired humidity-responsive liquid crystalline materials: from adaptive soft actuators to visualized sensors and detectors. Mater. Horiz. *10*, 2824-2844.
65. Chen, X., Li, Y., Wang, X., and Yu, H. (2022). Origami Paper-Based Stretchable Humidity Sensor for Textile-Attachable Wearable Electronics. ACS Appl. Mater. Interfaces *14*, 36227-36237.
66. Yu, K., Ji, X., Yuan, T., Cheng, Y., Li, J., Hu, X., Liu, Z., Zhou, X., and Fang, L. (2021). Robust Jumping Actuator with a Shrimp-Shell Architecture. Adv. Mater. *33*, 2104558.
67. Mu, J., Wang, G., Yan, H., Li, H., Wang, X., Gao, E., Hou, C., Pham, A.T.C., Wu, L., Zhang, Q., et al. (2018). Molecular-channel driven actuator with considerations for multiple configurations and color switching. Nat. Commun. *9*, 590.
68. Liu, Z., Wang, Z., Wang, S.-Q., Li, J., Chen, Y., Cheng, P., Zaworotko, M.J., and Zhang, Z. (2023). Porous Organic Cage with Water Vapor-Triggered Structural Transition for Actuation Applications. ACS Mater. Lett. *5*, 2139-2147.
69. Vannozzi, L., Yasa, I.C., Ceylan, H., Menciassi, A., Ricotti, L., and Sitti, M. (2018). Self-Folded Hydrogel Tubes for Implantable Muscular Tissue Scaffolds. Macromol. Biosci. *18*, 1700377.

70. Shi, Q., Liu, H., Tang, D., Li, Y., Li, X., and Xu, F. (2019). Bioactuators based on stimulus-responsive hydrogels and their emerging biomedical applications. NPG Asia Mater. *11*, 64. 10.1038/s41427-019-0165-3.
71. Lee, S., Lee, M., and Lee, J. (2021). Highly sensitive humidity-responsive actuator comprising aligned electrospun fibers containing metal–organic framework nanoparticles. Sens. Actuators B: Chem. *332*, 129520.
72. Zhou, J., Zhang, Y., Zhang, J., Zhang, D., Zhou, X., and Xiong, J. (2023). Breathable Metal–Organic Framework Enhanced Humidity-Responsive Nanofiber Actuator with Autonomous Triboelectric Perceptivity. ACS Nano. 10.1021/acsnano.3c04022.
73. Yang, M., Wang, S.-Q., Liu, Z., Chen, Y., Zaworotko, M.J., Cheng, P., Ma, J.-G., and Zhang, Z. (2021). Fabrication of Moisture-Responsive Crystalline Smart Materials for Water Harvesting and Electricity Transduction. J. Am. Chem. Soc. *143*, 7732-7739.
74. Andreo, J., Balsa, A.D., Tsang, M.Y., Sinelshchikova, A., Zaremba, O., Wuttke, S., and Chin, J.M. (2023). Alignment of Breathing Metal–Organic Framework Particles for Enhanced Water-Driven Actuation. Chem. Mater.
75. Xiang, C., Wang, W., Zhu, Q., Xue, D., Zhao, X., Li, M., and Wang, D. (2020). Flexible and Super-Sensitive Moisture-Responsive Actuators by Dispersing Graphene Oxide into Three-Dimensional Structures of Nanofibers and Silver Nanowires. ACS Appl. Mater. Interfaces *12*, 3245-3253.
76. Yan, D., Wang, Z., and Zhang, Z. (2022). Stimuli-Responsive Crystalline Smart Materials: From Rational Design and Fabrication to Applications. Acc. Chem. Res. *55*, 1047-1058.
77. Kim, T., Zhu, L., Al-Kaysi, R.O., and Bardeen, C.J. (2014). Organic Photomechanical Materials. ChemPhysChem *15*, 400-414.
78. Uribe-Romo, F.J., Doonan, C.J., Furukawa, H., Oisaki, K., and Yaghi, O.M. (2011). Crystalline Covalent Organic Frameworks with Hydrazone Linkages. J. Am. Chem. Soc. *133*, 11478-11481.
79. Das, G., Garai, B., Prakasam, T., Benyettou, F., Varghese, S., Sharma, S.K., Gándara, F., Pasricha, R., Baias, M., Jagannathan, R., et al. (2022). Fluorescence turn on amine detection in a cationic covalent organic framework. Nat. Commun. *13*, 3904.
80. Karimi, M.B., Hooshyari, K., Salarizadeh, P., Beydaghi, H., Ortiz- Martínez, V.M., Ortiz, A., Ortiz Uribe, I., and Mohammadi, F. (2021). A comprehensive review on the proton conductivity of proton exchange membranes (PEMs) under anhydrous conditions: Proton conductivity upper bound. Int. J. Hydrog. Energy *46*, 34413-34437.
81. Tao, S., Zhai, L., Dinga Wonanke, A.D., Addicoat, M.A., Jiang, Q., and Jiang, D. (2020). Confining H3PO4 network in covalent organic frameworks enables proton super flow. Nat. Commun. *11*, 1981.
82. Sasmal, H.S., Aiyappa, H.B., Bhange, S.N., Karak, S., Halder, A., Kurungot, S., and Banerjee, R. (2018). Superprotonic Conductivity in Flexible Porous Covalent Organic Framework Membranes. Angew. Chem. Int. Ed. *57*, 10894-10898.
83. Li, X.-M., Liu, J., Zhao, C., Zhou, J.-L., Zhao, L., Li, S.-L., and Lan, Y.-Q. (2019). Strategic hierarchical improvement of superprotonic conductivity in a stable metal–organic framework system. J. Mater. Chem. A *7*, 25165-25171.
84. Chandra, S., Kundu, T., Kandambeth, S., BabaRao, R., Marathe, Y., Kunjir, S.M., and Banerjee, R. (2014). Phosphoric Acid Loaded Azo (−N═N−) Based Covalent Organic Framework for Proton Conduction. J. Am. Chem. Soc. *136*, 6570-6573.
85. Ye, Y., Zhang, L., Peng, Q., Wang, G.-E., Shen, Y., Li, Z., Wang, L., Ma, X., Chen, Q.-H., Zhang, Z., and Xiang, S. (2015). High Anhydrous Proton Conductivity of Imidazole-Loaded Mesoporous Polyimides over a Wide Range from Subzero to Moderate Temperature. J. Am. Chem. Soc.*137*, 913-918.

86. Xu, H., Tao, S., and Jiang, D. (2016). Proton conduction in crystalline and porous covalent organic frameworks. Nat. Mater. *15*, 722-726.
87. Bian, S., Zhang, K., Wang, Y., Liu, Z., Wang, G., Jiang, X., Pan, Y., Xu, B., Huang, G., and Zhang, G. (2022). Charge Separation by Imidazole and Sulfonic Acid-Functionalized Covalent Organic Frameworks for Enhanced Proton Conductivity. ACS Appl. Energy Mater. *5*, 1298-1304.
88. Ranjeesh, K.C., Illathvalappil, R., Veer, S.D., Peter, J., Wakchaure, V.C., Goudappagouda, Raj, K.V., Kurungot, S., and Babu, S.S. (2019). Imidazole-Linked Crystalline Two-Dimensional Polymer with Ultrahigh Proton-Conductivity. J. Am. Chem. Soc. *141*, 14950-14954.
89. Chaloux, B.L., Ridenour, J.A., Johannes, M.D., and Epshteyn, A. (2022). Comparing Proton Conduction in Potassium and Ammonium Borosulfate—Isostructural Inorganic Polyelectrolytes Exhibiting High Proton Mobility. Adv. Energy Sustainability Res. *3*, 2200029.
90. Li, S., Liu, Y., Li, L., Liu, C., Li, J., Ashraf, S., Li, P., and Wang, B. (2020). Enhanced Proton Conductivity of Imidazole-Doped Thiophene-Based Covalent Organic Frameworks via Subtle Hydrogen Bonding Modulation. ACS Appl. Mater. Interfaces *12*, 22910-22916.
91. Ye, Y., Guo, W., Wang, L., Li, Z., Song, Z., Chen, J., Zhang, Z., Xiang, S., and Chen, B. (2017). Straightforward Loading of Imidazole Molecules into Metal–Organic Framework for High Proton Conduction. J. Am. Chem. Soc. *139*, 15604-15607.
92. Shigematsu, A., Yamada, T., and Kitagawa, H. (2011). Wide Control of Proton Conductivity in Porous Coordination Polymers. J. Am. Chem. Soc. *133*, 2034-2036.
93. Yang, F., Huang, H., Wang, X., Li, F., Gong, Y., Zhong, C., and Li, J.-R. (2015). Proton Conductivities in Functionalized UiO-66: Tuned Properties, Thermogravimetry Mass, and Molecular Simulation Analyses. Cryst. Growth. Des. *15*, 5827-5833.
94. Chandra, S., Kundu, T., Dey, K., Addicoat, M., Heine, T., and Banerjee, R. (2016). Interplaying Intrinsic and Extrinsic Proton Conductivities in Covalent Organic Frameworks. Chem. Mater. *28*, 1489-1494.
95. Pili, S., Rought, P., Kolokolov, D.I., Lin, L., da Silva, I., Cheng, Y., Marsh, C., Silverwood, I.P., García Sakai, V., Li, M., et al. (2018). Enhancement of Proton Conductivity in Nonporous Metal–Organic Frameworks: The Role of Framework Proton Density and Humidity. Chem. Mater. *30*, 7593-7602.
96. Sahoo, R., Mondal, S., Pal, S.C., Mukherjee, D., and Das, M.C. (2021). Covalent-Organic Frameworks (COFs) as Proton Conductors. Adv. Energy Mater. *11*, 2102300.
97. Lim, D.-W., and Kitagawa, H. (2020). Proton Transport in Metal–Organic Frameworks. Chem. Rev. *120*, 8416-8467.
98. Pal, S.C., and Das, M.C. (2021). Superprotonic Conductivity of MOFs and Other Crystalline Platforms Beyond 10−1 S cm−1. Adv. Funct. Mater. *31*, 2101584.
99. Ma, H., Liu, B., Li, B., Zhang, L., Li, Y.-G., Tan, H.-Q., Zang, H.-Y., and Zhu, G. (2016). Cationic Covalent Organic Frameworks: A Simple Platform of Anionic Exchange for Porosity Tuning and Proton Conduction. J. Am. Chem. Soc. *138*, 5897-5903.
100. Kumar, S., Hu, J., Pandikassala, A., Kurungot, S., Addicoat, M.A., and Szekely, G. (2023). Unlocking the potential of proton conductivity in guanidinium-based ionic covalent organic nanosheets (iCONs) through pore interior functionalization. Applied Mater. Today *33*, 101866.
101. Das, G., Nagaraja, S., Sridurai, V., Shinde, D.B., Addicoat, M., Prakasam, T., Gándara, F., Ravaux, F., Sharma, S.K., Nair, G.G., et al. (2019). Redox-Triggered Buoyancy and Size Modulation of a Dynamic Covalent Gel. Chem. Mater. *31*, 4148-4155.

102. Das, G., Ibrahim, F.A., Khalil, Z.A., Bazin, P., Chandra, F., AbdulHalim, R.G., Prakasam, T., Das, A.K., Sharma, S.K., Varghese, S., et al. Ionic Covalent Organic Framework as a Dual Functional Sensor for Temperature and Humidity. Small *n/a*, 2311064.
103. Mitra, S., Kandambeth, S., Biswal, B.P., Khayum M, A., Choudhury, C.K., Mehta, M., Kaur, G., Banerjee, S., Prabhune, A., Verma, S., et al. (2016). Self-Exfoliated Guanidinium-Based Ionic Covalent Organic Nanosheets (iCONs). J. Am. Chem. Soc. *138*, 2823-2828.
104. Jiang, S., Meng, L., Ma, W., Pan, G., Zhang, W., Zou, Y., Liu, L., Xu, B., and Tian, W. (2021). Dual-functional two-dimensional covalent organic frameworks for water sensing and harvesting. Mater. Chem. Front. *5*, 4193-4201.
105. El-Roz, M., Bazin, P., Birsa Čelič, T., Zabukovec Logar, N., and Thibault-Starzyk, F. (2015). Pore Occupancy Changes Water/Ethanol Separation in a Metal–Organic Framework—Quantitative Map of Coadsorption by IR. J. Phys. Chem. C *119*, 22570-22576.
106. Issa Hamoud, H., Wolski, L., Pankin, I., Bañares, M.A., Daturi, M., and El-Roz, M. (2022). In situ and Operando Spectroscopies in Photocatalysis: Powerful Techniques for a Better Understanding of the Performance and the Reaction Mechanism. Top. Curr. Chem. *380*, 37. 10.1007/s41061-022-00387-5.
107. Qian, C., Qi, Q.-Y., Jiang, G.-F., Cui, F.-Z., Tian, Y., and Zhao, X. (2017). Toward Covalent Organic Frameworks Bearing Three Different Kinds of Pores: The Strategy for Construction and COF-to-COF Transformation via Heterogeneous Linker Exchange. J. Am. Chem. Soc. *139*, 6736-6743.
108. Pielesz, A., and Włochowicz, A. (2001). Semiempirical infrared spectra simulations for some aromatic amines of interest for azo dye chemistry. Spectrochim. Acta - A: Mol. Biomol. Spectrosc. *57*, 2637-2646.
109. Fedoseeva, V.I., Pentin, Y.A., Krasnova, T.L., and Chernyshev, E.A. (1976). Vibrational spectra and the structure of trichloro- and trimethylphenoxysilanes. J. Appl. Spectrosc *24*, 46-50.
110. Lasch, P., and Noda, I. (2019). Two-Dimensional Correlation Spectroscopy (2D-COS) for Analysis of Spatially Resolved Vibrational Spectra. Appl. Spectrosc. *73*, 359-379. 10.1177/0003702818819880.
111. Sasmal, H.S., Aiyappa, H.B., Bhange, S.N., Karak, S., Halder, A., Kurungot, S., and Banerjee, R. (2018). Superprotonic conductivity in flexible porous covalent organic framework membranes. Angew. Chem. *130*, 11060-11064.
112. Yang, Y., He, X., Zhang, P., Andaloussi, Y.H., Zhang, H., Jiang, Z., Chen, Y., Ma, S., Cheng, P., and Zhang, Z. (2020). Combined Intrinsic and Extrinsic Proton Conduction in Robust Covalent Organic Frameworks for Hydrogen Fuel Cell Applications. Angew. Chem. Int. Ed. *59*, 3678-3684.
113. Shukla, J., Illathvalappil, R., Kumar, S., Chorol, S., Pandikassala, A., Kurungot, S., and Mukhopadhyay, P. (2022). Synthesis of a Highly Electron-Deficient, Water-Stable, Large Ionic Box: Multielectron Accumulation and Proton Conductivity. Organic Letters *24*, 3038-3042.
114. Agmon, N. (1995). The Grotthuss mechanism. Chem. Phys. Lett. *244*, 456-462.
115. Aftab, S., Shah, A., Nisar, J., Ashiq, M.N., Akhter, M.S., and Shah, A.H. (2020). Marketability Prospects of Microbial Fuel Cells for Sustainable Energy Generation. Energy & Fuels *34*, 9108-9136.

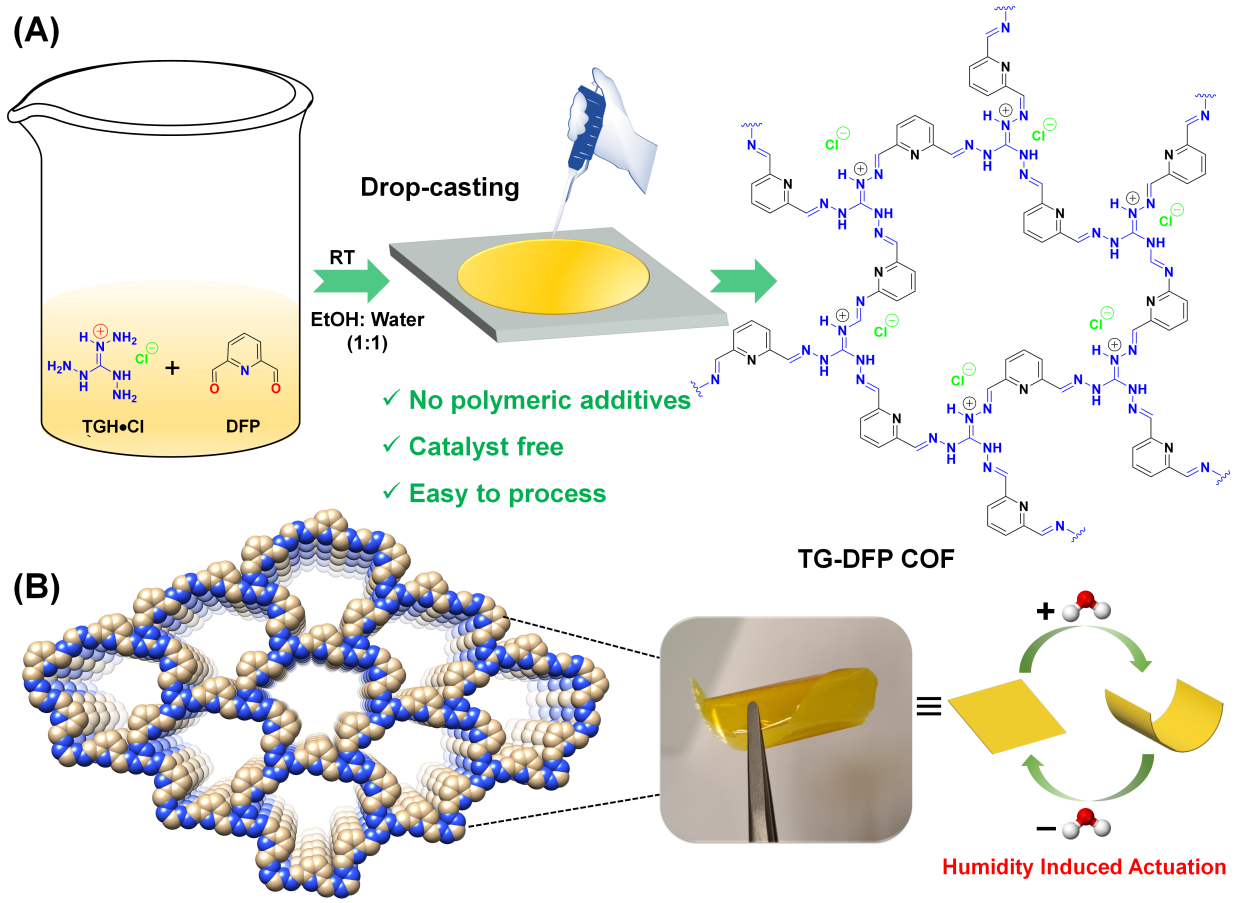

Figure 1. (A) Schematic illustration for the synthesis of theTG-DFP COF film at room temperature in ethanol : H_2O (1:1). (B) Simulated crystal structure shown in a spacing filling eclipsed model (Cl^- counterions have been omitted for clarity) in top view and cartoon representations showing the mechanical motion in response to humidity.

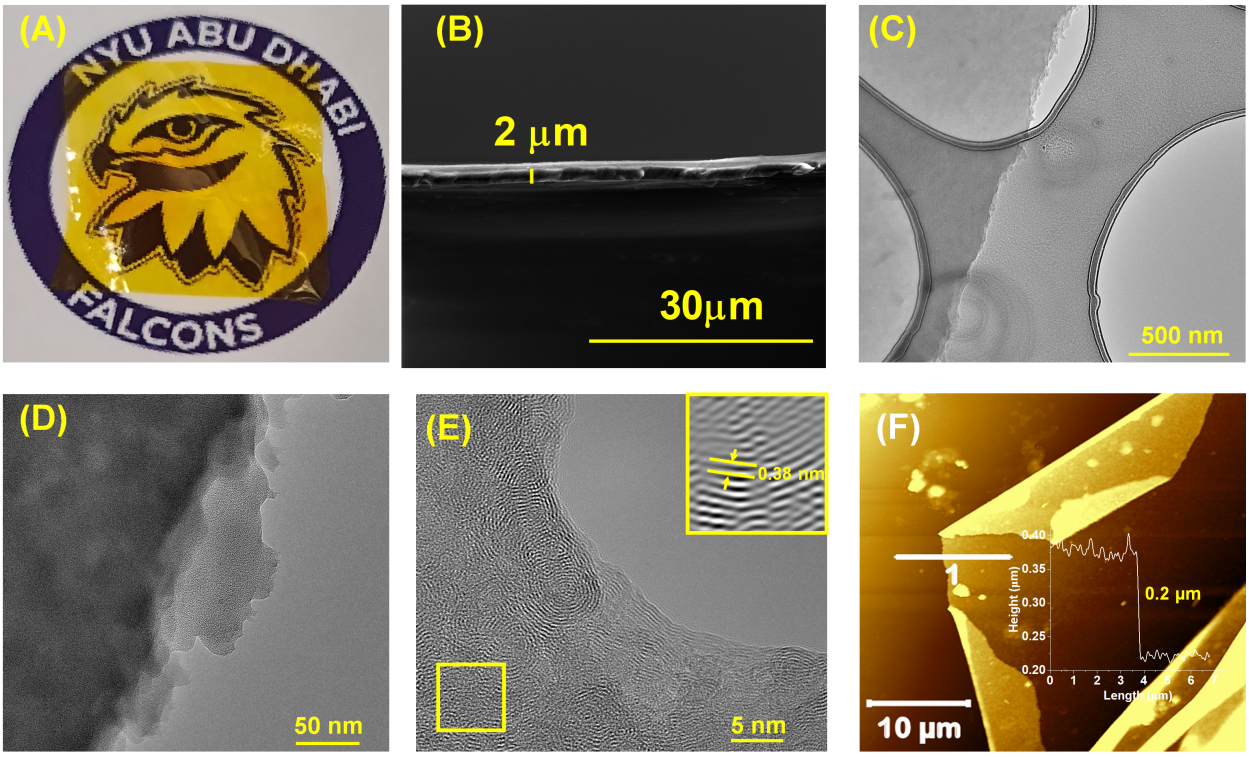

Figure 2. Microscopy analysis of the TG-DFP COF film: (A) Photograph demonstrating the transparency of the TG-DFP COF film (2 cm × 2 cm) when placed over a standard white paper featuring a printed university logo. (B) Cross-sectional SEM image of the TG-DFP COF film. C-E) HRTEM images of the film at different magnifications. F) AFM images of the TG-DFP COF (the height profile is shown in the inset).

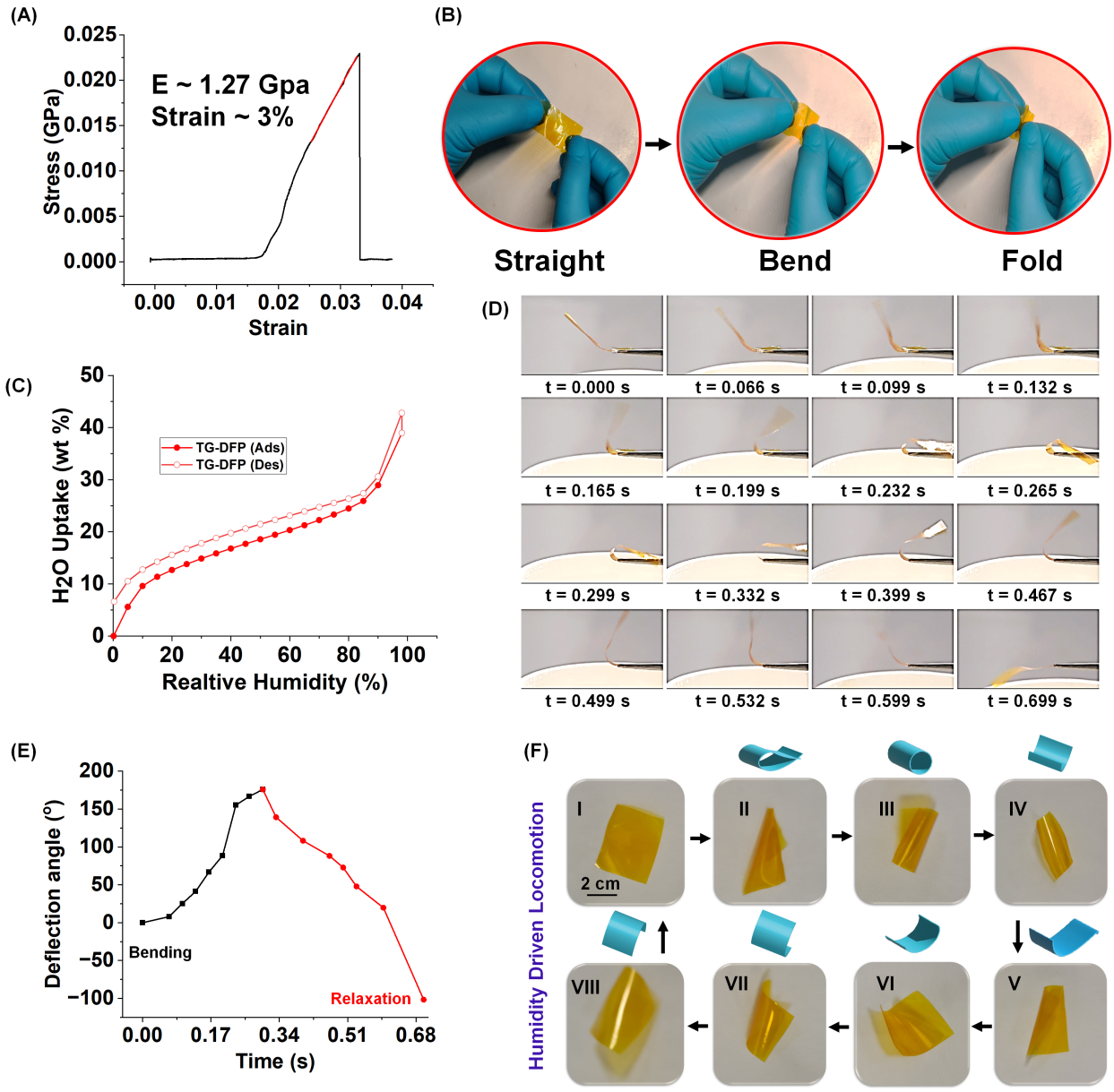

Figure 3. (A) Investigation of the stress-strain behavior of the TG-DFP COF film under dynamic mechanical conditions; (B) Bending resistance test of free-standing TG-DFP COF film with a thickness of 2 μm; (C) Dynamic water vapor sorption (DVS) isotherm of TG-DFP COF powder at 298 K (solid circles adsorption, empty circles desorption); (D) High-speed snapshots of the motions of TG-DFP COF film in response to humidity during a complete curling-to-straight motion cycle; (E) Plot of time ss deflection angle of the TG-DFP COF film during actuation; (F) Mechanism of flipping locomotive motion by the TG-DFP COF film after exposure to humidity.

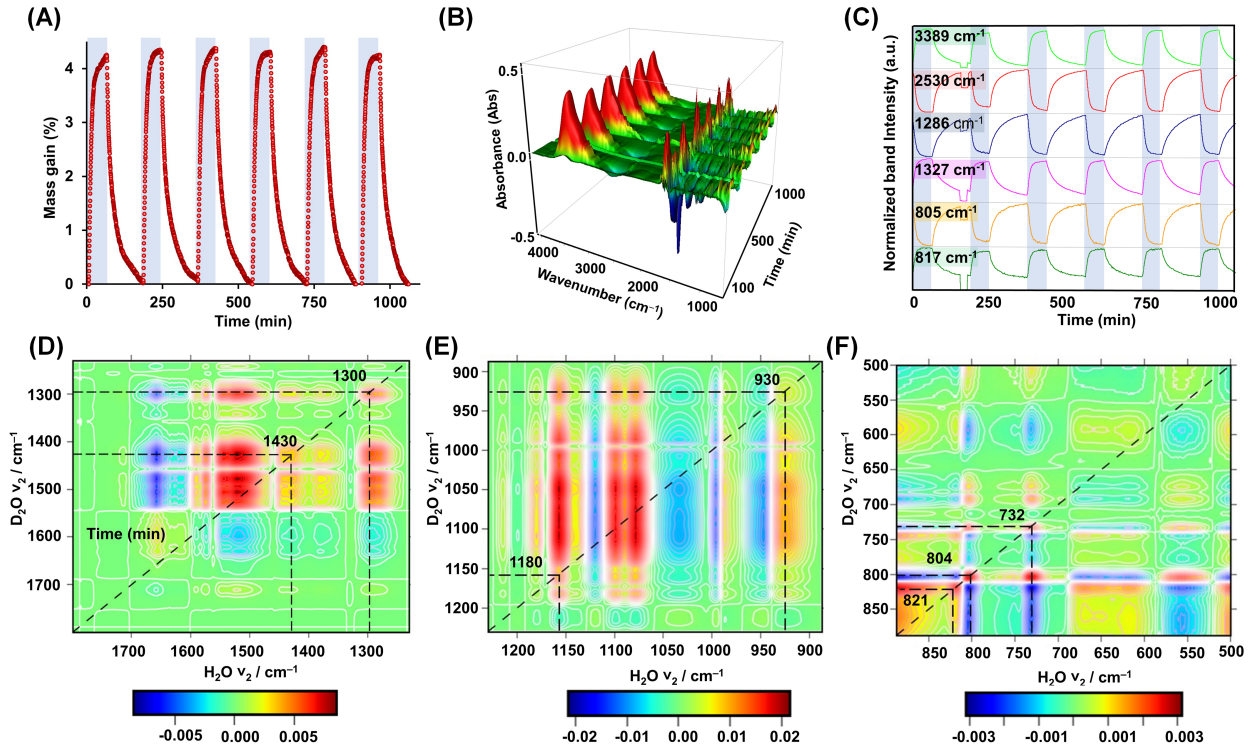

Figure 4. Thermogravimetry coupled to FTIR (AGIR) experiments: (A) Evolution of the mass gain (in percent) of the TG-DFP COF film during various wet (RH=4%)/dry cycles at 25 °C under Ar carrier gas flow (25 cm^3/min). (B) and (C) correspond to the 3D and 2D plots of the evolution of the IR spectra and bands, respectively, of the film during the various cycles. The red and green colors in (C) correspond to the negative and positive evolution of corresponding vibration bands, respectively. The spectra were subtracted from the spectrum of the film at steady state under dry Ar. (D-F) Two-dimensional correlation FTIR spectroscopy (2DCOS) analyses of H_2O/D_2O-dependent IR spectra of the TG-DFP film versus the RH in various vibrational regions (for clarity).

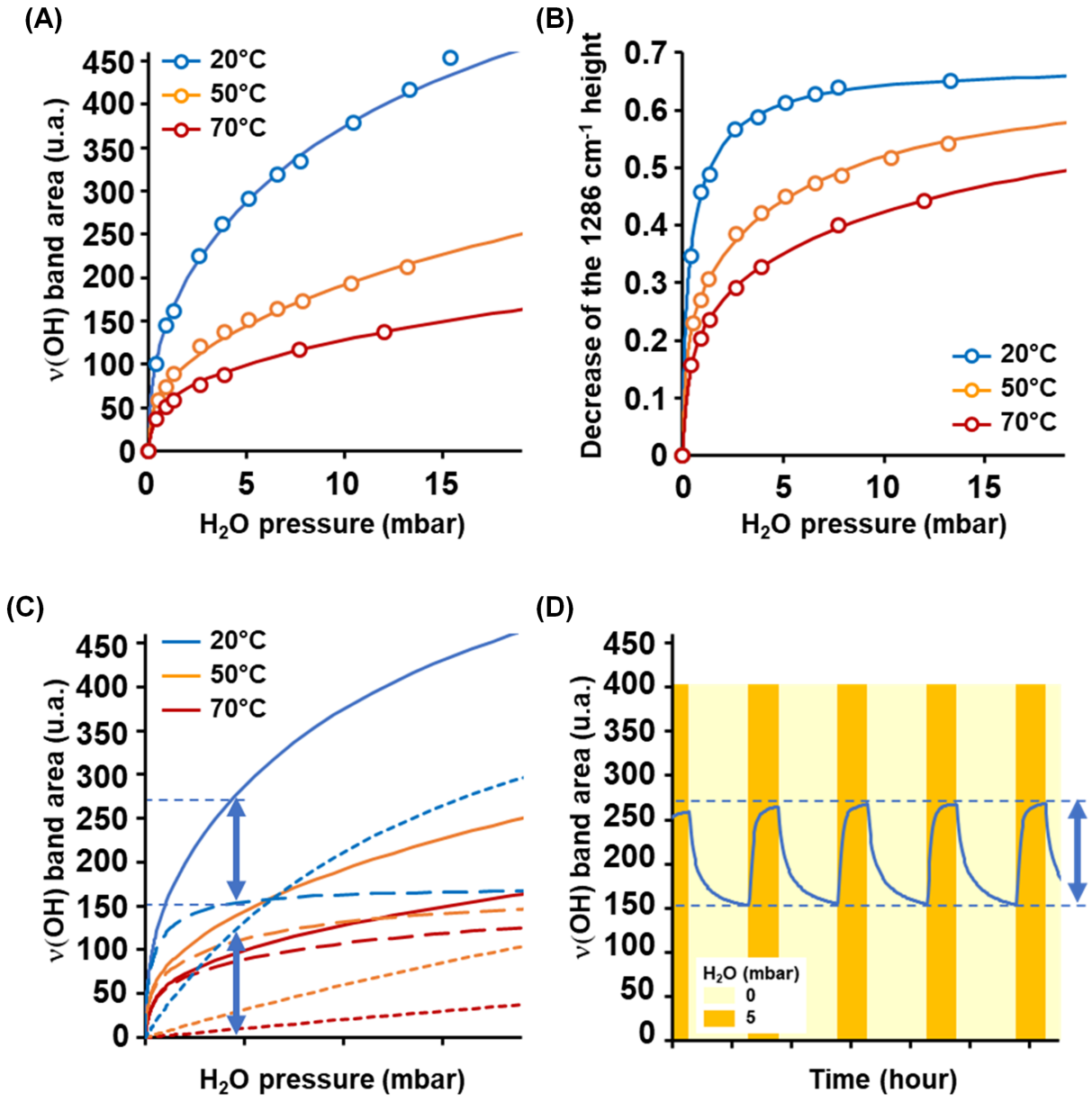

Figure 5. (A) Optical adsorption isotherms of H_2O on TG-DFP (area of the v(OH) band at ~3380 cm^{-1} versus H_2O pressure); (B) Evolution of the v(CN) structural band's intensity of the film (at 1286 cm^{-1}; in absolute value) versus H_2O pressure. (C) v(OH) band area versus H_2O pressure (modeled curves). Large dotted line: curve proportional to the 1286 cm^{-1} band height (identical factor for 20, 50 and 70 °C), small dotted line: Langmuir model and solid line: sum of the previous two. (D) Cycles of H_2O (5 mbar/1h) / H_2O (0 mbar/2h) in Ar (20 cm^3 min^{-1}) at 20°C. For (A), (B) and (C): experimental data (circle) and modeling

curve (solid line). The vertical arrow in (C) and D) indicates the range of v(OH) band area variation during cycles at 20 ºC and 5 mbar of H_2O.

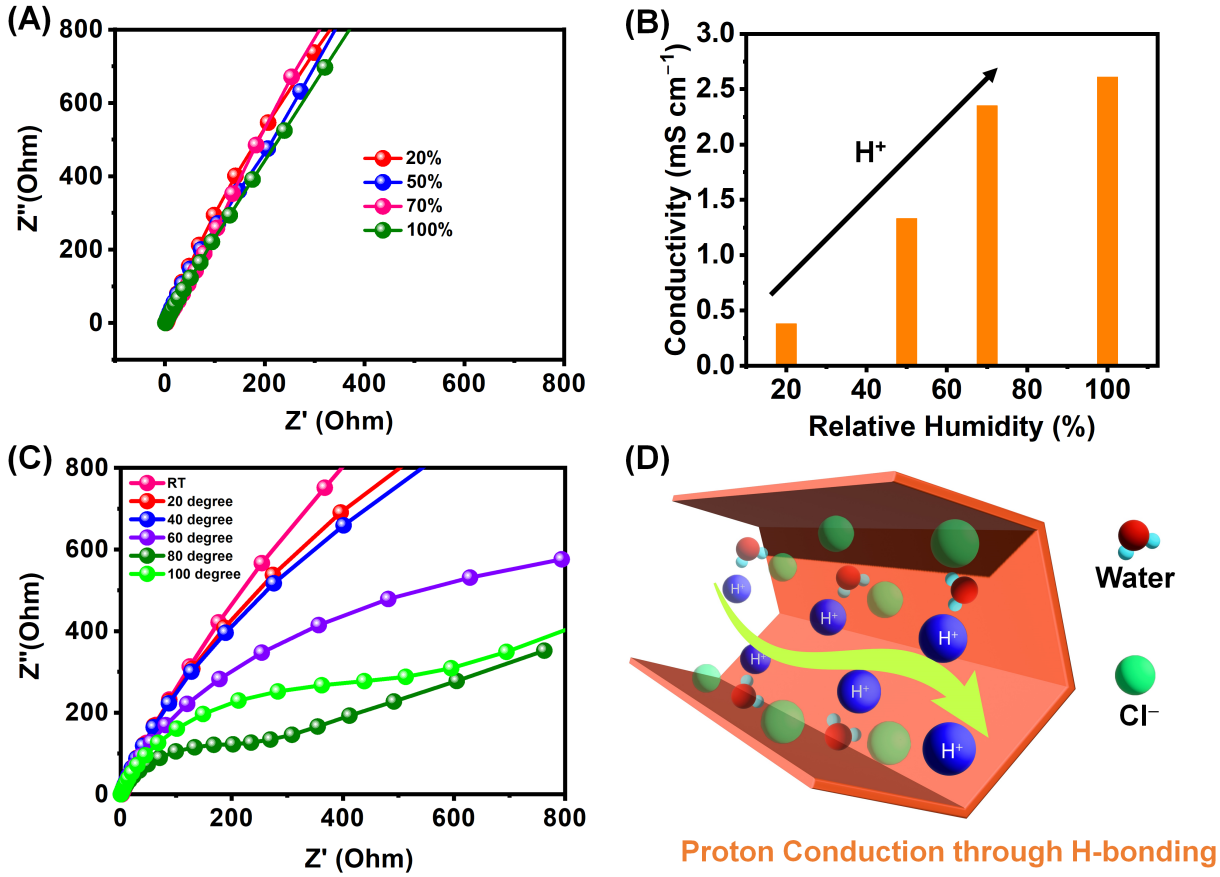

Figure 6. (A) Nyquist plot of TG-DFP COF film under varying humidity levels; (B) Plot of relative humidity vs proton conductivity; (C) Temperature-dependent proton conductivity measurements for the TG-DFP COF film (20–100 °C); (D) Graphical representations depicting the suggested pathway for proton conduction.

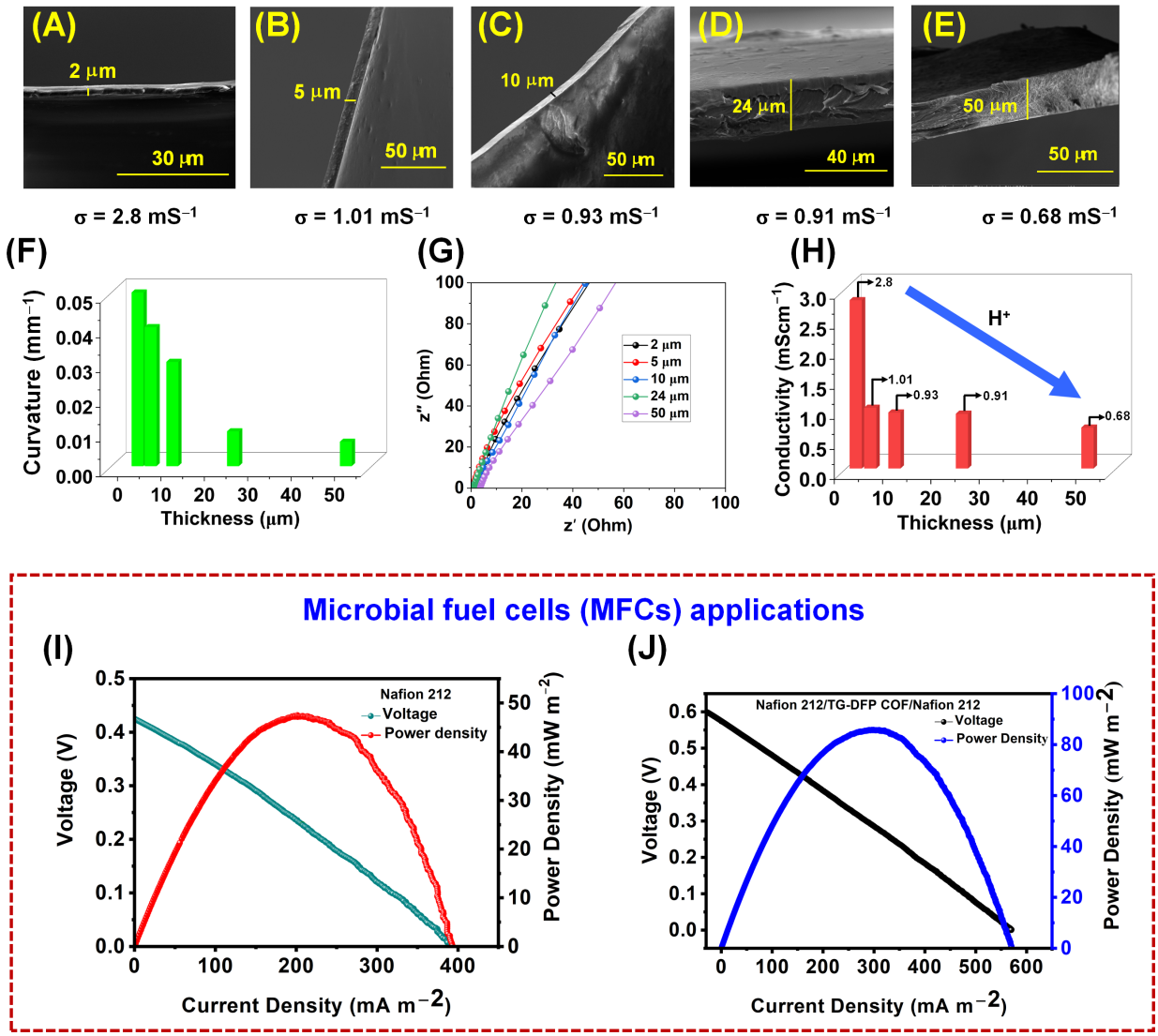

Figure 7. A-E) Cross-sectional SEM images of TG-DFP COF film at different thickness, F) The plot of the maximum bending curvature of the TG-DFP COF film (2cm) as a function film thickness (μm), G-H) Thickness dependent proton conductivity analysis of TG-DFP COF film, Microbial fuel cells (MFCs) experiment for (I) Nafion 212 membrane and (J) Nafion 212/TG-DFP COF/Nafion 212).

Supplemental videos

Video S1: Mechanical flexibility of the TG-DFP COF film.

Video S2: Actuation cycles in response to humidity.

Video S3: Locomotive motion of TG-DFP COF film.

Video S4: Actuation behavior of the TG-DFP COF film in presence of acetone.

Video S5: Actuation behavior of the TG-DFP COF film in response to dichloromethane and water.

Video S6: Actuation behavior of the TG-DFP COF film in response to ethanol.

TOC

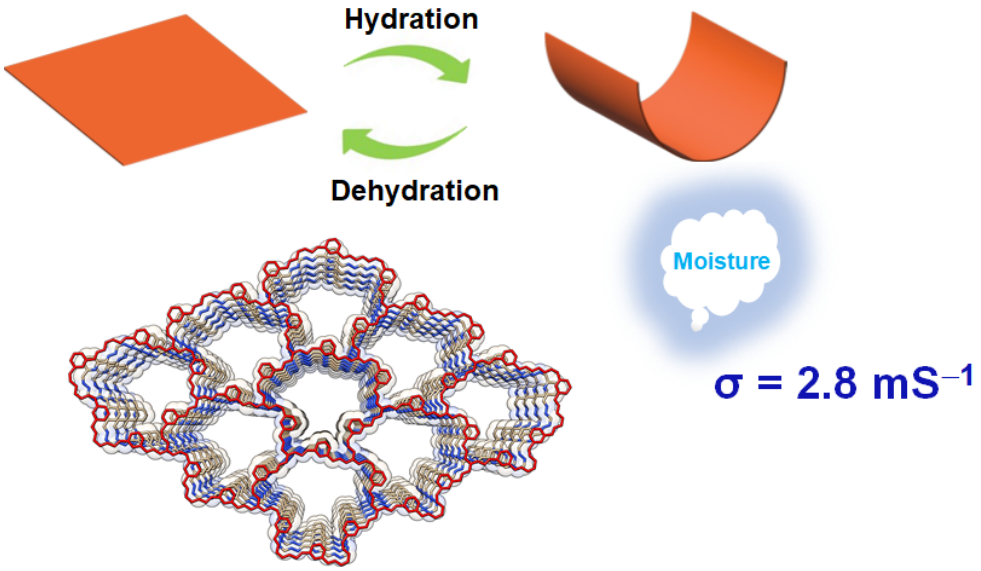

Humidity induced actuation and proton conduction